Peer-reviewed version available at Materials 2018, 11, 2343; doi:10.3390/ma11122343

Effect of SLM process parameters on the quality of Al Alloy parts; Part I: powder characterization, density, surface roughness, and dimensional accuracy

Ahmed H. Maamoun *[1)], *Yi F. Xue*[1)], *Mohamed A. Elbestawi* [1)], *Stephen C. Veldhuis*[1)]

[1)]*McMaster University*, Department of Mechanical Engineering,
1280 Main Street West Hamilton, ON, Canada, L8S 4L7

Abstract

Additive manufacturing (AM) of high strength Al alloys promises to enhance the performance of critical components related to various aerospace and automotive applications. The key advantage of AM is its ability to generate lightweight, robust, and complex shapes. However, the characteristics of the as-built parts may represent an obstacle to satisfy the part quality requirements. The current study investigates the influence of selective laser melting (SLM) process parameters on the quality of parts fabricated from different Al alloys. A design of experiment (DOE) is used to analyze relative density, porosity, surface roughness, and dimensional accuracy according to the interaction effect between the SLM process parameters. The results show a range of energy densities and SLM process parameters for the AlSi10Mg and Al6061 alloys needed to achieve "optimum" values for each performance characteristic. A process map is developed for each material by combining the optimized range of SLM process parameters for each characteristic to ensure good quality of the as-built parts. The second part of this study investigates the effect of SLM process parameters on the microstructure and mechanical properties of the same Al alloys. This comprehensive study is also aimed at reducing the amount of post-processing needed.

Keywords: Additive Manufacturing; Selective Laser Melting; AlSi10Mg; Al6061; SLM process parameters; Powder characterization; Density, Surface topology; Dimensional accuracy

* *Corresponding author contact: maamouna@mcmaster.ca; elbestaw@mcmaster.ca*

1. Introduction

High-strength aluminum alloys (Al alloys) are typical used for the production of lightweight critical components for a variety of applications in space, aerospace, automotive, military, and biomedical fields [1]. Additive manufacturing (AM) offers additional flexibility in the design and manufacturing of parts, particularly the ability to fabricate complex geometries without the need for custom tools [2]. SLM offers superior dimensional accuracy and material quality of the fabricated parts [3].

SLM is a layer-by-layer process, in which the laser beam selectively melts the powder layer according to slices generated from the three-dimensional designed model. SLM possesses rapid melting and solidification rates, and thus is applicable for a narrow selection of materials according to their coefficient of thermal expansion (CTE). In addition, optimization of SLM process parameters of Al alloys is hampered by part defects due to energy loss in the laser beam projected to the powder bed surface. The quality of Al alloys produced by SLM could be influenced by the chemical composition and CTE of the material used. Galy et al. [4] showed that porosity, hot cracking, anisotropy, and surface quality are the principal defects of Al alloy parts. They also demonstrated that selection of SLM process parameters and the laser beam energy loss due to Al reflectivity are the primary causes of porosity and hot crack formation.

Some of the SLM process parameters can be controlled, such as laser power, scan speed, hatch spacing, and powder layer thickness. The energy density is a function of these parameters. Optimization of the SLM process parameters is an essential step for controlling material characteristics and the quality of the fabricated parts. Sufiiarov et al. [5] showed that using a 30

µm powder layer thickness could result in a higher strength and lower elongation for Inconel 718 than the values obtained with a 50 µm layer thickness. Nguyen et al. [6] also studied the effect of the powder layer thickness within a range from 20 to 50 µm. Their results showed that as the thickness of the powder layer diminishes, part density and dimensional accuracy increase. Cheng et al. [7] investigated the effect of scanning strategy on the stress and deformation of parts. Their results showed that minimum stress and deformation values are obtained using a layer orientation strategy with an angle of 45˚ or 67˚. The powder feedstock quality also represents an essential parameter that might affect part characteristics. Sutton et al. [8] reported that the powder morphology, microstructure, and chemical characteristics could change depending on the production method such as gas, water, or plasma atomization techniques. This could generate a difference in quality between the parts produced using different feedstock powders [9,10].

Various studies [11–15] utilized a design of experiment (DOE) approach to investigate the effect of SLM process parameters on AlSi10Mg part quality, by evaluating their density, surface roughness, and dimensional accuracy. Read et al. [12] used the response surface methodology (RSM) to evaluate the influence of SLM process parameters on part porosity. Their study was limited by the use of a laser power up to 200 W. The results showed that minimum porosity was obtained at a critical energy density of 60 J/mm^3. Abouelkhair et al. [13] used one factor at a time (OFAT) method to optimize the SLM process parameters for producing dense parts. They achieved an optimum combination of laser power, scan speed, and hatch spacing which resulted in a 99.77% relative density. Hitzler et al. [15] demonstrated that the surface roughness of the as-built samples varies according to their position on the build plate. They also concluded that the increase of energy density resulted in higher values of roughness on the surface of the side faces, compared to the

roughness values measured on the top surface. Calignano et al. [14] used the Taguchi method to investigate the effect of the SLM process parameters on the surface roughness of the parts. They found that the laser scan speed has a significant influence on the surface roughness. Lower surface roughness was obtained using a scan speed of 900 mm/s, 120W laser power, and 0.1 mm hatch spacing. Han et al. [16] reported that a decrease in surface roughness, combined with an increase of the laser scan speed, results in better dimensional accuracy. It is worthwhile to note that the previous studies used the DOE within a range of laser power up to 200 W. However, the post-processing treatment is also considered to be an essential stage of reducing the defects inside the as-built parts. This in turn, raises the final production cost of the parts [17–19]. Consequently, optimization of the SLM process parameters has a significant role in optimizing the steps of the manufacturing process. This might lead to a cost-effective process for specific applications which are compatible with the characteristics of the as-built parts.

In general, Al6061 is seldom used for SLM. Fulcher et al. [20] reported that Al6061 parts have a lower dimensional accuracy compared to the AlSi10Mg parts due to higher CTE. High strength Al alloys such Al6061 and Al7075 series have low Mg and Si content which might result in hot cracking and formation of large columnar grains [21]. Louvis et al. [22] reported that low relative density parts of Al6061 might be produced via SLM due to the effect of oxide formation inside these parts. This might result from the relatively low laser power used, (100W) which may not be enough to achieve complete melting. In general, more research is required to evaluate the effect of SLM process parameters on the as-built Al6061 characteristics such as density, surface roughness, and dimensional accuracy. In addition, the effect of Si content requires further investigation aimed at optimizing the process parameters.

In this study, a comprehensive experimental study using the DOE approach is performed to evaluate the influence of the SLM process parameters on the quality of as-built Al alloys. Part I of the manuscript focuses on investigating the density, surface topology, and dimensional accuracy of AlSi10Mg and Al6061. SLM process parameters are selected over a wide range of laser power, scanning speed, and hatch spacing values. Part characteristics are evaluated for various SLM parameters to develop a process map which displays the effect of Si content on part quality. Part II will cover the impact of the SLM process parameters on the microstructure and mechanical properties of the same Al alloys. This work aims to investigate the limits of SLM in fabricating critical components for aerospace industry using these alloys. In particular, the current research is focused on producing high-quality metallic optics and optomechanical components to improve the performance of telescopes and laser systems.

2. Experimental procedure

2.1 Material

Powder characterization was performed according to ASTM F3049-14. The powders chemical composition was evaluated using Energy X-ray dispersive Spectroscopy (EDS). The powder size distribution was measured using laser diffraction by dispersing the powder in water. The powder morphology was investigated using a Scanning Electron Microscope (SEM). A diffractometer equipped with a cobalt sealed tube source and an area detector was used to obtain the X-ray diffraction (XRD) phase pattern for both powders.

2.2 Design of experiment

Preprints (www.preprints.org) | NOT PEER-REVIEWED | Posted: 2 November 2018 doi:10.20944/preprints201811.0025.v1

Peer-reviewed version available at Materials 2018, 11, 2343; doi:10.3390/ma11122343

A DOE was developed to evaluate the response of the SLM process parameters and the volumetric energy density with respect to the as-built parts quality. The volumetric energy density is defined as follows:

$$E_d = \frac{\mathrm{P}}{\mathrm{V}_s * D_h * \mathrm{T}_l}$$

Where the E_d is the energy density (J/mm^3), P is the laser beam power (W), V_s is the laser scan speed (mm/s), D_h is the hatch spacing between scan passes, and T_l is the deposited layer thickness (µm). The OFAT method was used to analyze the performance of the AlSi10Mg samples. Eight different samples were produced with six replications for each. Several SLM parameters were selected to build the AlSi10Mg samples as listed in Table 1, with a constant layer thickness of 30 µm. The effect of the laser power, scan speed, hatch spacing, and energy density on the as-built part characteristics are evaluated with regression analysis.

Table 1: The SLM process parameters used for building the AlSi10Mg samples.

Sample#	P (W)	V_s (mm/s)	D_h (mm)	E_d (J/mm^3)
AS1	370	1000	0.19	65
AS2	370	1300	0.15	63.2
AS3	370	1300	0.19	50
AS4	350	1300	0.19	47.2
AS5	370	1500	0.19	43.3
AS6	300	1300	0.19	40.5
AS7	370	1300	0.25	38
AS8	200	1300	0.19	27

A full factorial DOE was developed using the response surface over a wide range of SLM parameters. Two sets of three SLM parameters (laser power, scanning speed, and hatch spacing) were selected as presented in Table 2. Three samples for each SLM parameters group were

Preprints (www.preprints.org) | NOT PEER-REVIEWED | Posted: 2 November 2018 doi:10.20944/preprints201811.0025.v1

Peer-reviewed version available at Materials 2018, 11, 2343; doi:10.3390/ma11122343

fabricated for a total of 48 samples. The energy density (E_d) for the Al6061 study was selected within a higher range (40-125 J/mm^3) compared to the E_d used for AlSi10Mg (27-65 J/mm^3). This is due to the higher reflectivity of laser power for Al6061, which results in less energy absorption by the powder particles. The overlap of SLM parameters for some samples of AlSi10Mg and Al6061 enabled investigation of each material at equal parameters.

Table 2: The SLM process parameters applied for fabricating the Al6061 samples.

Sample#	P (W)	V_s (mm/s)	D_h (mm)	E_d (J/mm^3)	Sample#	P (W)	V_s (mm/s)	D_h (mm)	E_d (J/mm^3)
1A	370	1000	0.1	123.3	**11A**	370	800	0.15	102.8
2A	300	1000	0.1	100	**12A**	350	800	0.15	97.2
3A	370	1300	0.1	95	**13A**	370	800	0.19	81.1
4A	300	1300	0.1	76.9	**14A**	350	800	0.19	76.8
5A	370	1000	0.19	65	**15A**	370	1300	0.15	63.2
6A	300	1000	0.19	52.6	**16A**	350	1300	0.15	59.8
7A	370	1300	0.19	50	**17A**	370	1300	0.19	50
8A	300	1300	0.19	40.5	**18A**	350	1300	0.19	47.2

2.3 SLM process parameters

The AlSi10Mg and Al6061 parts were fabricated by an EOSINT M290 machine equipped with a 400W Yb-fiber laser using a 100 µm laser beam diameter. The same layer thickness of 30 µm and layer orientation angle of 67˚ were selected for all samples undergoing strip scan, and 0.02 mm laser beam offset. The build chamber was vacuumed with Argon to reduce the oxygen content below 0.1%, and thus the possibility of oxide formation in the produced parts. All samples were fabricated as 15 mm cubes according to the SLM parameters listed in Tables 1 and 2. A preheating technique was applied to the build platform at 200 ˚C before starting the build to minimize the thermal residual stresses (by reducing the thermal gradient between the deposited layers).

2.4 Sample characterization method

In Part I of this study, part characterization focuses on relative density, internal porosity, surface roughness, and dimensional accuracy. Archimedes method was used to measure the density of the as-built cubes for both AlSi10Mg and Al6061 samples. The relative density was also evaluated after sample surface polishing to investigate the percentage of internal porosity. Density measurement via water displacement, according to ASTM B962-17, was performed with an electronic Densimeter (MD-200S).

Surface roughness measurements were performed according to ASTM D7127-17 with a Mitutoyo SJ-410 surface tester. Five measurements at intervals of 4.5 mm were conducted on the cubic specimen's top surface, and their average was taken at each location. A light microscope (Alicona Infinite Focus G5) was used to capture the surface texture of some of the AlSi10Mg and Al6061 samples. The area tested is 10 mm x 10 mm using a 10x magnification lens, and surface roughness also was measured to validate the values obtained by the mechanical stylus.

The measurement of geometric dimensions and tolerances (GD&T) was conducted with a Mitutoyo CRYSTA-Apex S544 Coordinate Measuring Machine (CMM) which includes an SP25M stylus. This machine has a resolution of 0.1μm within a working zone of 500mm x 400mm x 400mm. The tested surface was probed at 10 measurement points along each sample's face. Flatness, perpendicularity, and parallelism were measured for all sample faces except the bottom.

3. Results and discussion

3.1 Powder Characterization

Preprints (www.preprints.org) | NOT PEER-REVIEWED | Posted: 2 November 2018 doi:10.20944/preprints201811.0025.v1

Peer-reviewed version available at Materials 2018, 11, 2343; doi:10.3390/ma11122343

The characteristics of the gas atomized AlSi10Mg and Al6061 powder, supplied by the LPW Company, were examined according to ASTM F3049-14. The powder was sieved with a 75 µm mesh before being characterized. The morphology of both powders was detected using SEM as illustrated in Figure 1. The SEM observations show a relatively higher percentage of elongated or irregular shape particles in the AlSi10Mg powder compared to the spherical particles detected for the same alloy provided by a different supplier as reported by Maamoun et al.[17,18]. The Al6061 also shows a greater percentage of spherical particles compared to the AlSi10Mg powder shown in Figure 1. The existence of irregular or elongated particles might reduce powder flowability and homogeneity of the powder layer distribution, and thus negatively affect the quality and density of the fabricated parts [9]. The combination of a wide range of fine and coarse particles could increase the powder packing density, but it reduces the flowability due to the effect of powder cohesion and inter-particle forces [9]. The weight percentage of the chemical elements of both powders were detected with EDS, as listed in Table 3. The results reveal higher Si content inside the AlSi10Mg powder, and relatively lower weight percentage of Mg, Cu, and Fe compared to the Al6061 powder. The influence of this difference in chemical composition, in addition to the effect of powder particle shape, on the characteristics of the as-built parts, will be discussed in the following sections.

Table 3: The EDS analysis of the Al6061 and AlSi10Mg powders chemical composition.

Element	Si	Mg	Cu	Fe	Al
Al6061 wt%	1.2	0.77	0.32	0.90	Balance
AlSi10Mg wt%	11.34	0.28	0.08	0.32	Balance

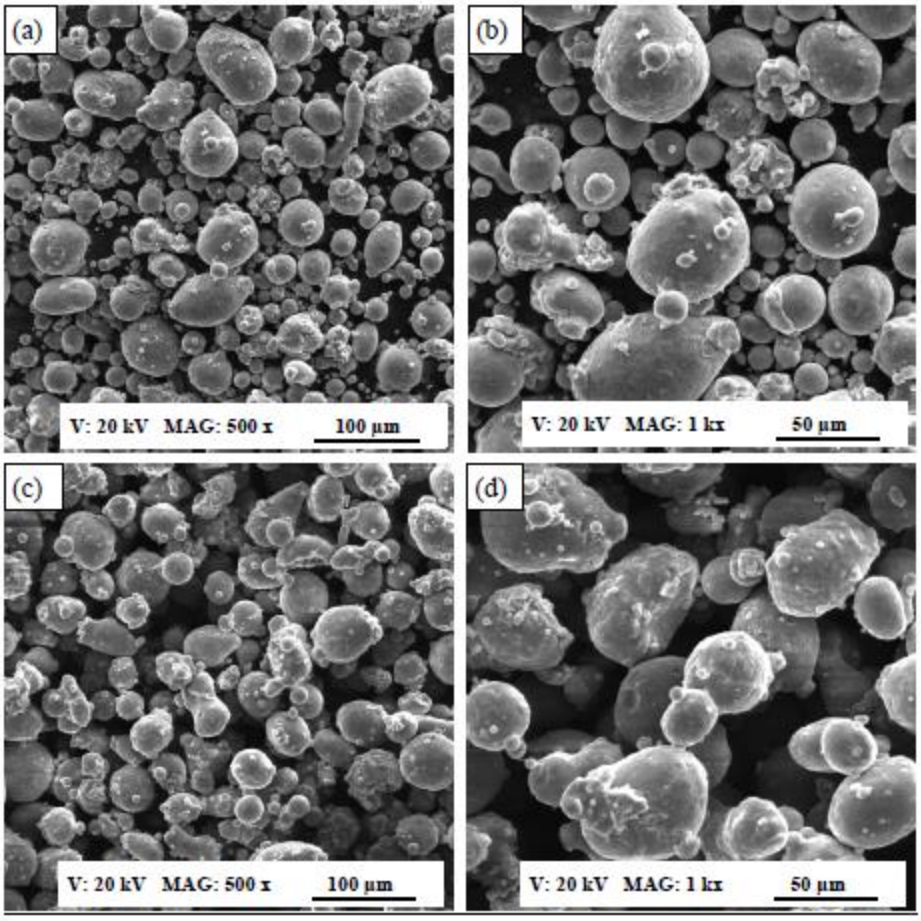

Figure 1: The SEM observations of the powder morphology: a, b) Al6061 powder; c, d) AlSi10Mg powder.

182

183 Figure 2 illustrates the profile PSD of AlSi10Mg and Al6061 powder attributes with a
184 positively skewed profile. This PSD profile could achieve a better surface quality and higher
185 density compared to negatively skewed and Gaussian distribution grades by increasing the laser
186 energy absorption [9,23]. The quantitative data of PSD presented in Table 4 show that the particle
187 size ranges from 12 to 110 µm for the AlSi10Mg, and from 12 to 120 µm for the Al6061 powder.
188 These results indicate the presence of larger sized particles compared to the mesh size used for
189 sieving. This might be related to the elongated particles detected with a smaller cross-section which
190 permits filtration through the mesh during sieving. Table 4 data also illustrate that for AlSi10Mg

Preprints (www.preprints.org) | NOT PEER-REVIEWED | Posted: 2 November 2018 doi:10.20944/preprints201811.0025.v1

Peer-reviewed version available at Materials 2018, 11, 2343; doi:10.3390/ma11122343

191 and Al6061 powder, 90% of the particles are less in size than the sieving mesh (75 µm) where
192 D(0.9) is measured as 66.55 and 71.92 µm respectively.

Table 4: The values measured for the particle size distribution of the Al6061 and AlSi10Mg powders.

Sample Name		D(0.1)	D(0.5)	D(0.9)
Al6061 Powder	Diameter (µm)	22.83	41.27	71.92
AlSi10Mg Powder		23.16	39.62	66.55

193

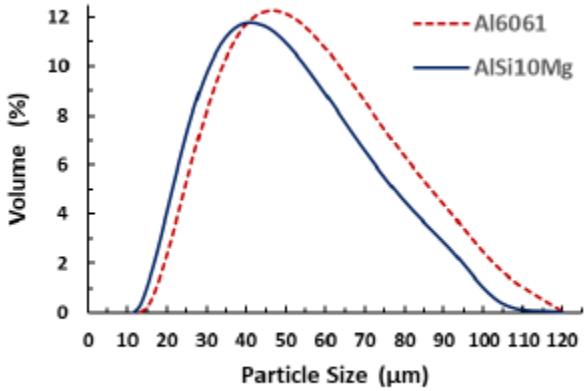

Figure 2: Particle size distribution of the Al6061 and AlSi10Mg powders.

194

195 The XRD phase patterns of AlSi10Mg and Al6061powder were detected as shown in Figure
196 3. The Al and Si peaks were identified according to the Joint Committee on Powder Diffraction
197 Standards (JCPDS) patterns of 01-089-2837, 01-089-5012 respectively. The low-intensity of the
198 Si peaks in the Al6061 phase pattern, is due to its small weight percentage inside that alloy. For
199 the AlSi10Mg powder, the higher intensity of Si peaks and the slight shift of the Al peaks to the
200 left indicates a lower solubility of Si in AlSi10Mg compared to Al6061[24].

Preprints (www.preprints.org) | NOT PEER-REVIEWED | Posted: 2 November 2018 doi:10.20944/preprints201811.0025.v1

Peer-reviewed version available at Materials 2018, 11, 2343; doi:10.3390/ma11122343

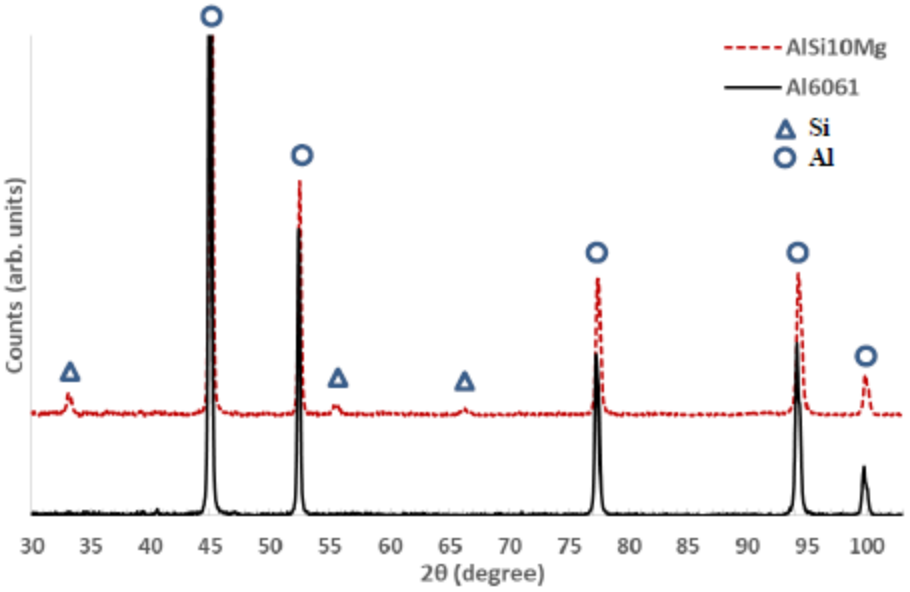

Figure 3: The XRD phase patterns of the Al6061 and AlSi10Mg powders.

201

202 **3.2 Relative Density**

203 Figure 4 shows the effect of energy density on the formation of pores inside the as-built
204 AlSi10Mg part. The results show that the low energy density of 27 J/mm^3 in the AS8 sample, could
205 cause significant keyhole porosity due to the lack of fusion of powder particles during the SLM
206 process as shown in Figure 4(a). The keyhole pores are observed along the building direction
207 within the layer boundaries, which have an irregular elongated shape due to the low energy density.
208 The keyhole pores might form either due to insufficient energy delivered to the powder particles
209 or due to the entrapment of gas bubbles between the interlayers during laser scanning [25]. The
210 keyhole pore size reaches 200 µm and gradually decreases as the energy density increases, until
211 disappearing when the energy density value exceeds 50 J/mm^3. Inside the keyhole pores, partially
212 melted particles are visible, as shown in Figure 4(d). This may occur due to trapping of the
213 consolidated powder inside the keyhole pore as a result of the low energy incident on the powder

particle surface. However, the spherical hydrogen pores or metallurgical pores are observed within 10 µm size at 50 J/mm^3 as shown in Figure 4(b, e). The average size of these spherical pores tends to grow by more than 20 µm at 65 J/mm^3 as illustrated in Figure 4(c, f). The mechanism of pore formation at high fusion rates might be related to the pores existing inside the gas atomized powder particles [4]. They may also result from the balling phenomena where the melted powder failed to wet the previously deposited layer [26].

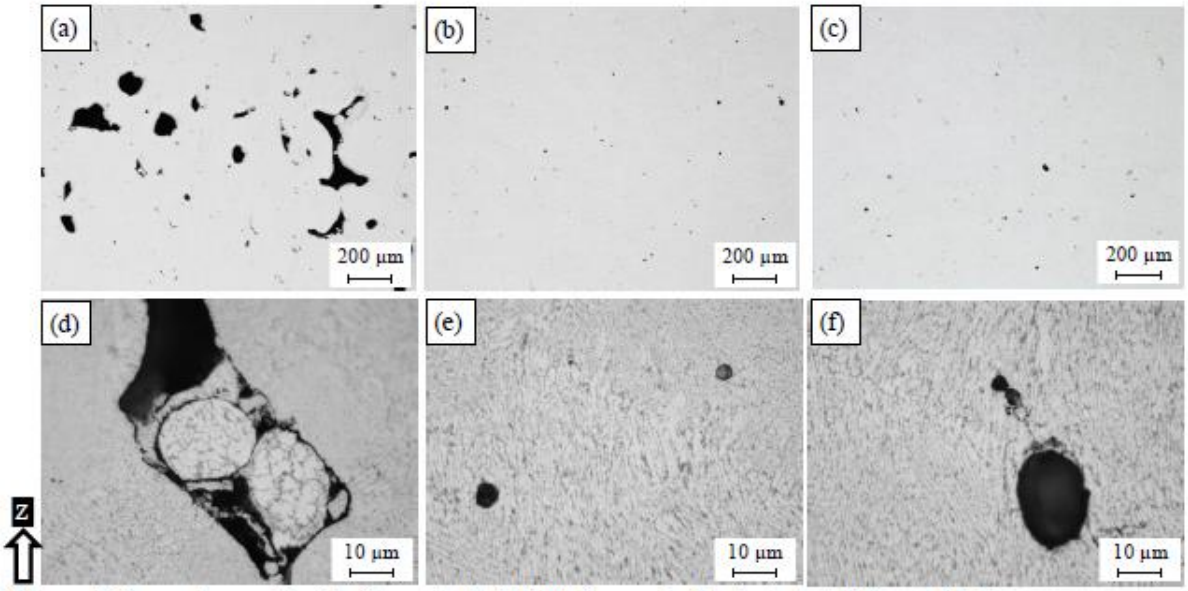

Figure 4: Pores observed inside the as-built AlSi10Mg sample fabricated at different SLM parameters; a, d) AS8, b, e) AS3, c) AS1.

The mechanism of pore formation inside the as-built AlSi10Mg samples according to the SLM process parameters presented in Figure 4, is validated after evaluating the relative density. Figure 5 illustrates the map developed by the regression model generated from the DOE analysis. This map describes the effect of laser power, scan speed, hatch spacing and energy density on the relative density of the as-built AlSi10Mg parts. The results show the optimum range of process parameters which allow the least amount of spherical and keyhole pores to reach the highest

possible relative density value of the part. The energy density value between 50 to 60 J/mm^3 produces a high relative density reaches 99.7%. Beyond this range, the relative density diminishes either due to the lack of fusion at the lower energy density, balling formation at the higher energy density, or hydrogen gases trapped inside the powder particles. It is worthwhile to note that higher values of the as-built part density could be obtained according to optimized SLM process parameters compared to the values reported by different literature studies [12,27–29]. In order to evaluate the internal porosity inside the as-built cube samples, their outer sides were polished before the relative density was re-measured. As shown in Figure 5, the relative density of the polished samples reaches 99.9 at an energy density of 50 J/mm^3 with a 0.1-1% reduction in porosity. By comparing the relative density between the as-built and polished sample, it can be concluded that an increase in hatch spacing or scan speed parameters significantly increases the porosity on the sample surface, as illustrated in Figure 5. This effect might result from the reduction of the material solidification rate at a higher scan speed and hatch spacing due to heat accumulation. The effect of laser power indicates a significant impact of the growth of the melting rate and energy on the relative density of the as-built part. It is worth noting that the porosity percentage could be reduced after preheating the build platform prior to the sample build as reported by Siddique et al. [30].

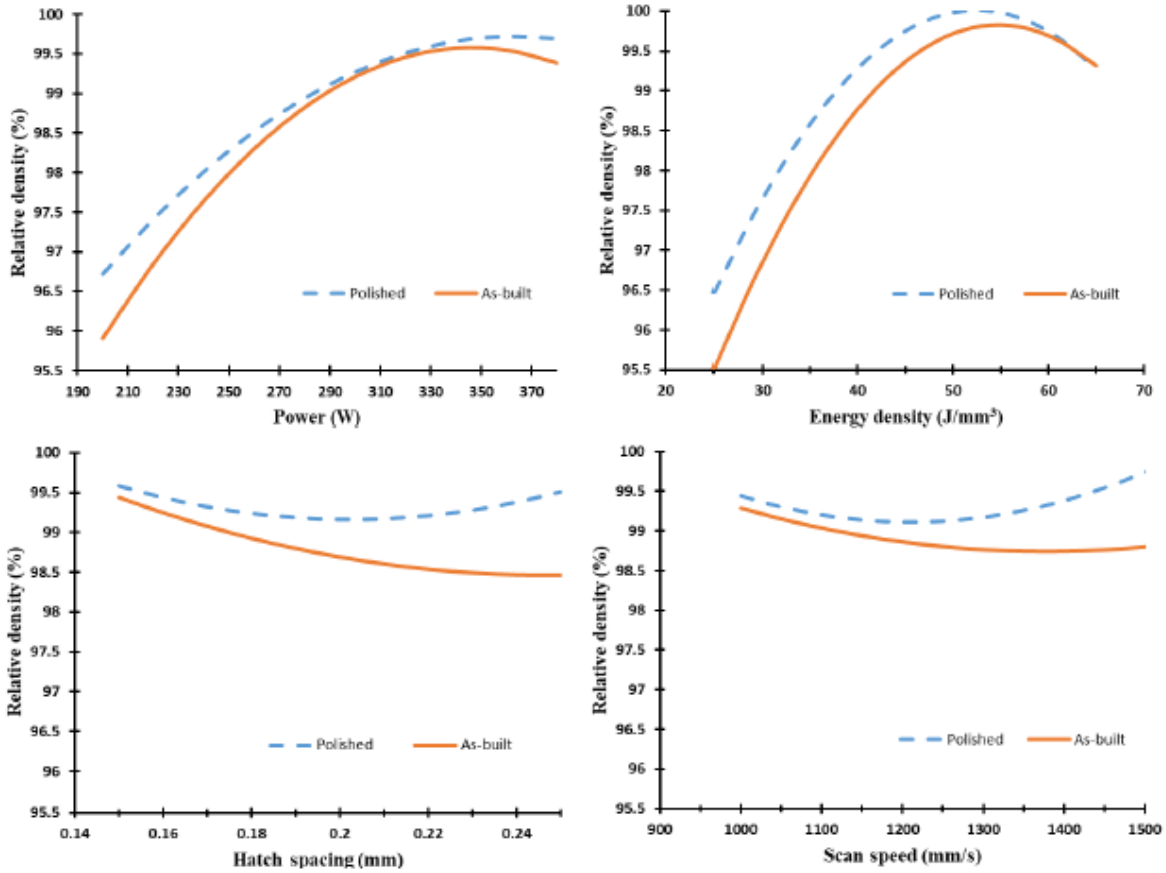

Figure 5: Influence of the SLM process parameters on relative density of the as-built AlSi10Mg samples.

Figure 6 shows the microscopic observations of the polished as-built Al6061 samples fabricated at different SLM process parameters listed in Table 2. Different sizes of micro-cracks are observed between the samples along the Z-direction and the XY-plane. As shown in Figure 6, a lower porosity percentage is observed compared to the as-built AlSi10Mg samples. The keyhole pores are also reduced until they are hardly noticeable, with the exception of some spherical hydrogen pores. However, the relative density is relatively lower than that of the AlSi10Mg samples due to the presence of micro-cracks. The size of these micro-cracks depends on the thermal gradient between the deposited layer in addition to the COE of the alloy, and this is also

affected by changing the SLM process parameters applied. Figure 6 (a-c) shows the longitudinal microcracks formed along the Z-direction. The different size of these cracks is obtained according to the applied SLM parameters. The smallest size and density of the cracks were observed after the applied energy density reached 102.8 J/mm^3 in the 1A sample. However, no specific trend was detected between the energy density and the density of cracks, which is in agreement with Debroy et al. [31]. As illustrated in Figure 6(d-f), the micro-cracks along the XY plane are shaped as semi-closed loops similar in form to an equiaxed grain, but they are not entirely closed or sharp-edged. The results show that the laser scan speed is the leading parameter affecting crack formation. The crack density, along with the building direction, increases along with energy density from 40.5 to 76.9 J/mm^3 at the same scan speed (1300 mm/s) as shown in Figure 6 (a, b) respectively. However, the crack density displayed in Figure 6(c), is significantly reduced at a higher energy density (102.8 J/mm^3) with a lower scan speed of 800 mm/s. Consequently, the scan speed has a more substantial effect on hot crack formation than the applied energy density, since it controls the rate of solidification. The size of the semi-closed cracks formed in the XY plane tends to grow alongside scan speed reduction as noted in Figure 6(d-f). The indents presented in Figure 6 (d-f) are formed during the microhardness measurement that will be covered in Part II of this study.

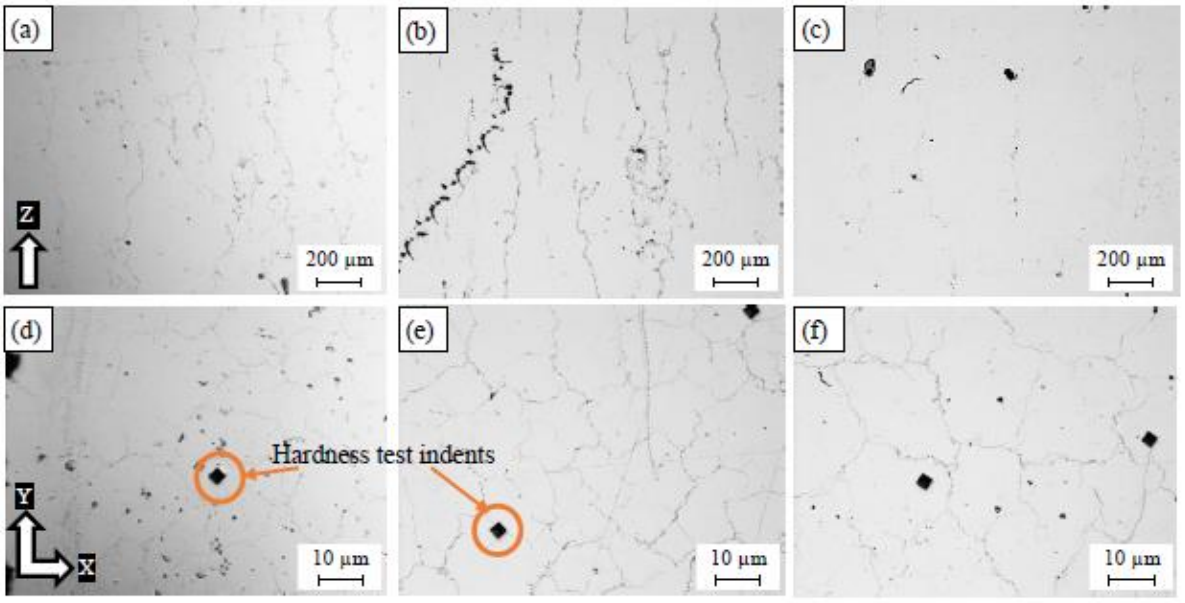

Figure 6: Pores observed inside the as-built Al6061 samples processed through different SLM parameters; a, d) 8A, b, e) 4A, c) 1A.

Figure 7 presents the plots generated via the DOE analysis using the effect of the two combined process parameters on the relative density of the as-built part. It can be concluded that relative density tends to increase along with laser power and energy density, while a lower rate of the laser scan speed leads to denser parts. A significant relationship can be seen between laser power and scan speed. A relative density average of 98.2% ± 0.5 is measured according to the selected process parameters where the maximum relative density reaches 98.72%. These plots validate the trend obtained from the microscopic observations in Figure 6 and confirm the effect of the laser scan speed on crack formation and relative density. The cracks observed inside the as-built parts could result from the hot crack phenomena which occur during material solidification, due to combined chemical composition of the material. Kou et al. [32] reported that adding filler materials during welding to the Al alloys susceptible to crack formation, could eliminate the cracks

and enhance the alloy's weldability. This explains the crack free structure obtained in the as-built AlSi10Mg parts, which have a high Si content compared to Al6061.

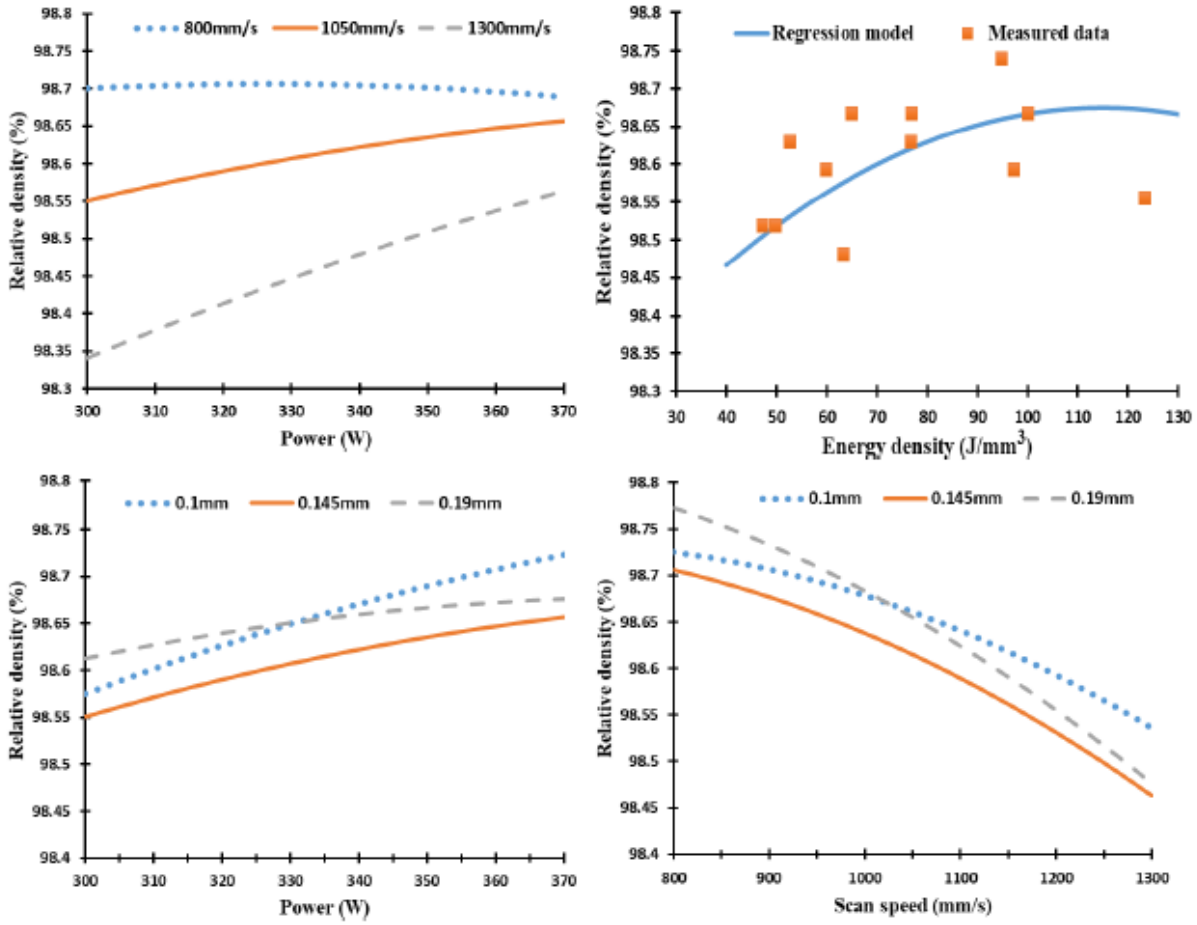

Figure 7: The SLM process parameters effect on relative density of the as-built Al6061 samples.

3.3 Surface topology

The surface topology analysis of the as-built AlSi10Mg and Al6061 parts is conducted with SEM, displaying the 3D surface texture, and mapping the surface roughness relationship with SLM process parameters according to the DOE analysis regression model. The surface defects of the as-built AlSi10Mg parts are exhibited in Figure 8 for different samples alongside energy density

increase. Figure 8(a, d) shows the rough surface obtained from the AS8 sample fabricated using a low energy density of 27 J/mm^3. According to SEM observations, this high roughness results from surface pores forming due to a lack of fusion and partially melted powder adhering to the surface. As shown in Figure 8(b, e), an increase of energy density in the AS3 sample to 49.9 J/mm^3, improves surface roughness by eliminating noticeable surface pores and by reducing the density of the partially melted powder attached to the surface. However, the tracks of laser scanning are still visible with the commencement of balling phenomena. Figure 8 (c, f) shows a better surface on the AS1 sample after applying a higher energy density of 63 J/mm^3. This eliminates the tracks of laser scanning, but the balling effect is still present. The balling phenomena occurs at higher energy density levels due to the surface tension generated around the melted powder particles. This represents an obstacle to the wetting of the underlying substrate layer by the melted powder [31]. It is also worthwhile to note that the effect of the balling phenomena increases as energy density exceeds 65 J/mm^3. As a result, the part build fails due to the detachment of the powder layer, which had melted on the top of the underlying layer.

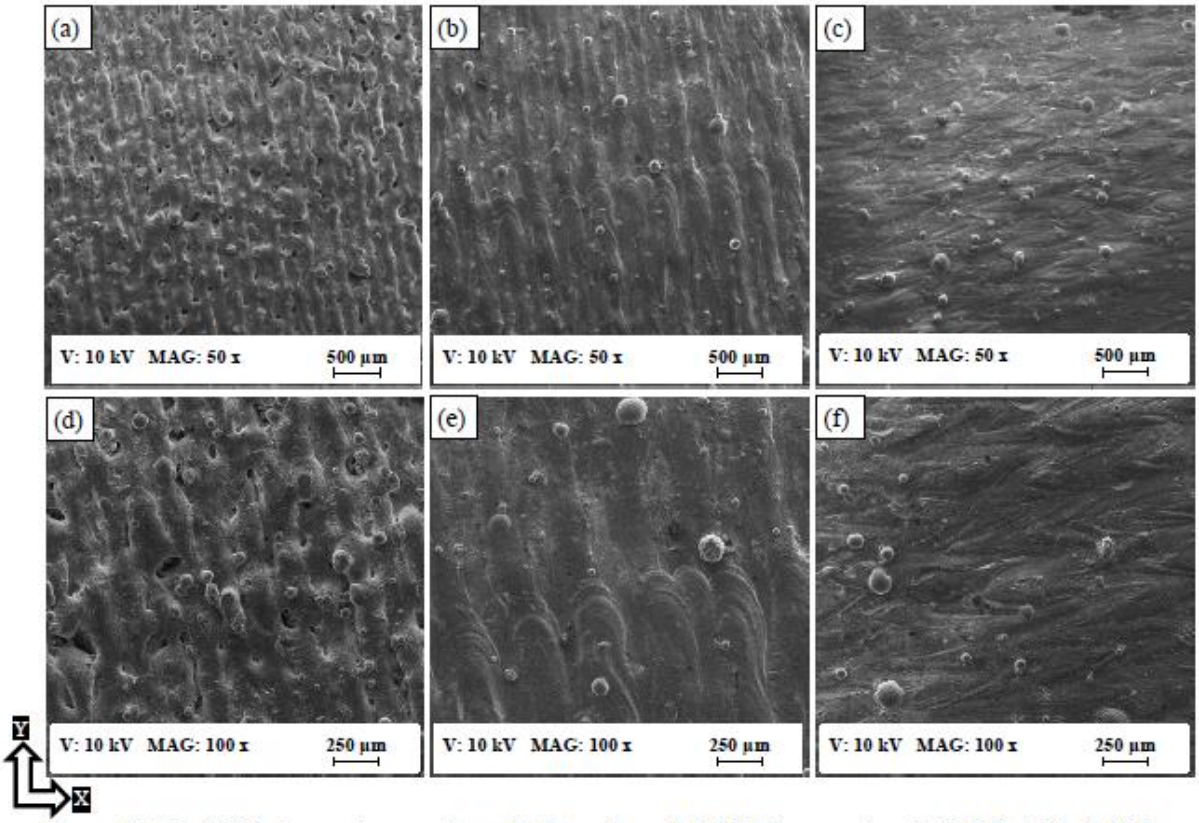

Figure 8: The SEM observations on the as-built surface of AlSi10Mg samples; a) AS8, b) AS3, c) AS1.

Figure 9 exhibits the 3D surface texture of the as-built AlSi10Mg samples; the results show a significant improvement of the surface roughness alongside an increase of the energy density up to a specific limit. As shown in Figure 9(a), applying a low energy density of 27 J/mm^3 resulted in a rough texture with an average of 15 µm surface roughness. As illustrated in Figure 9(b), the surface roughness decreased to 10 µm at a relatively high energy density of 40.5 J/mm^3. The surface roughness continues to decrease until reaching the lowest value of 4.5 µm at an energy density of 65 J/mm^3 as presented in Figure 9(c, d).

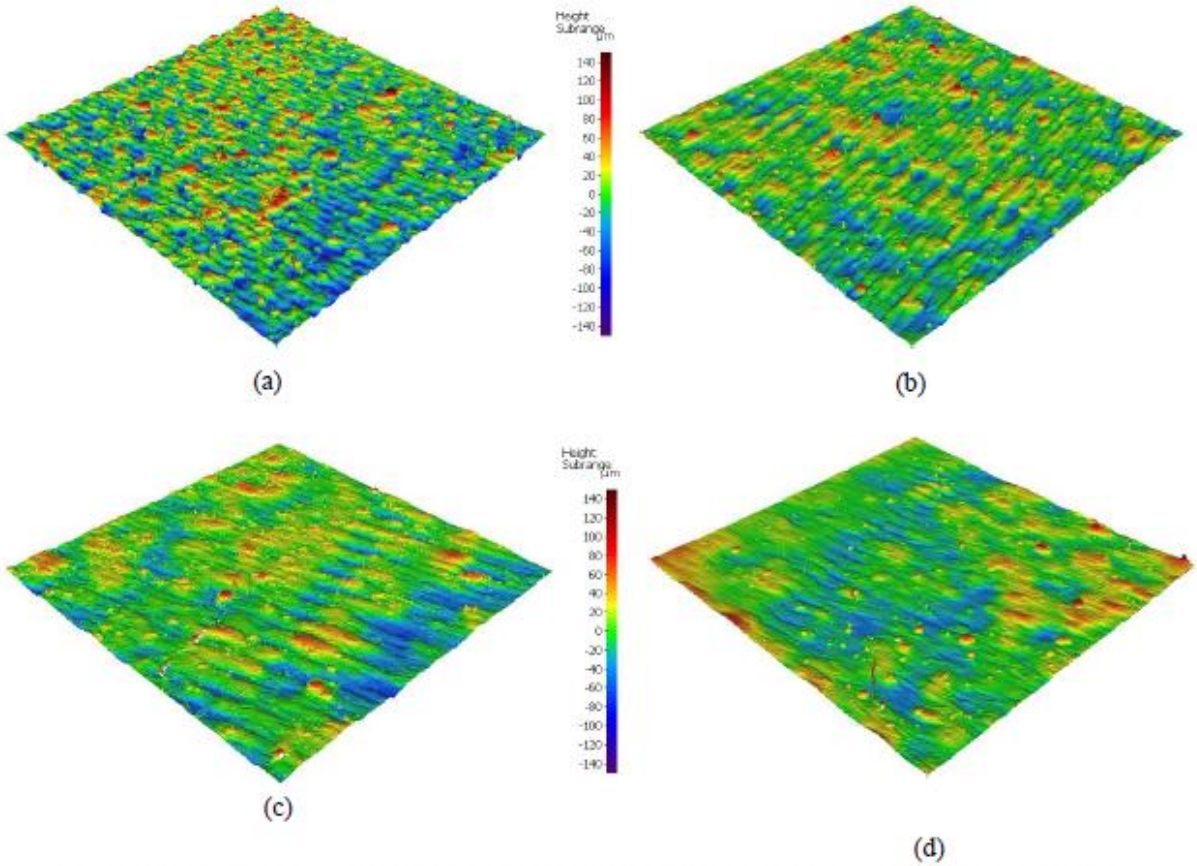

Figure 9: The 3D surface texture of the as-built AlSi10Mg samples; a) AS8, b) AS6, c) AS3, d) AS1.

311

312 The mapping of the SLM process parameter effect on the surface roughness of the as-built
313 AlSi10Mg parts is illustrated in Figure 10. The regression model generated by the energy density
314 effect on surface roughness shows a good agreement with the measured values. The laser power
315 effect reveals the same trend as the energy density influence on the samples' surface roughness.
316 This map also shows that the increasing of hatch spacing value resulted in a more rough surface
317 due to decreasing overlap between the melted tracks, which agrees with the trend presented by
318 Foster et al. [33]. Surface roughness also increases with the laser scan due to the reduction of the
319 molten layer solidification rate. Superior surface roughness of 4.5 µm is achieved under an E_d of

320 65 J/mm^3 at 370W laser power, 1000 mm/s scan speed, and 0.19 mm hatch spacing, which is in
321 good agreement with the regression model.

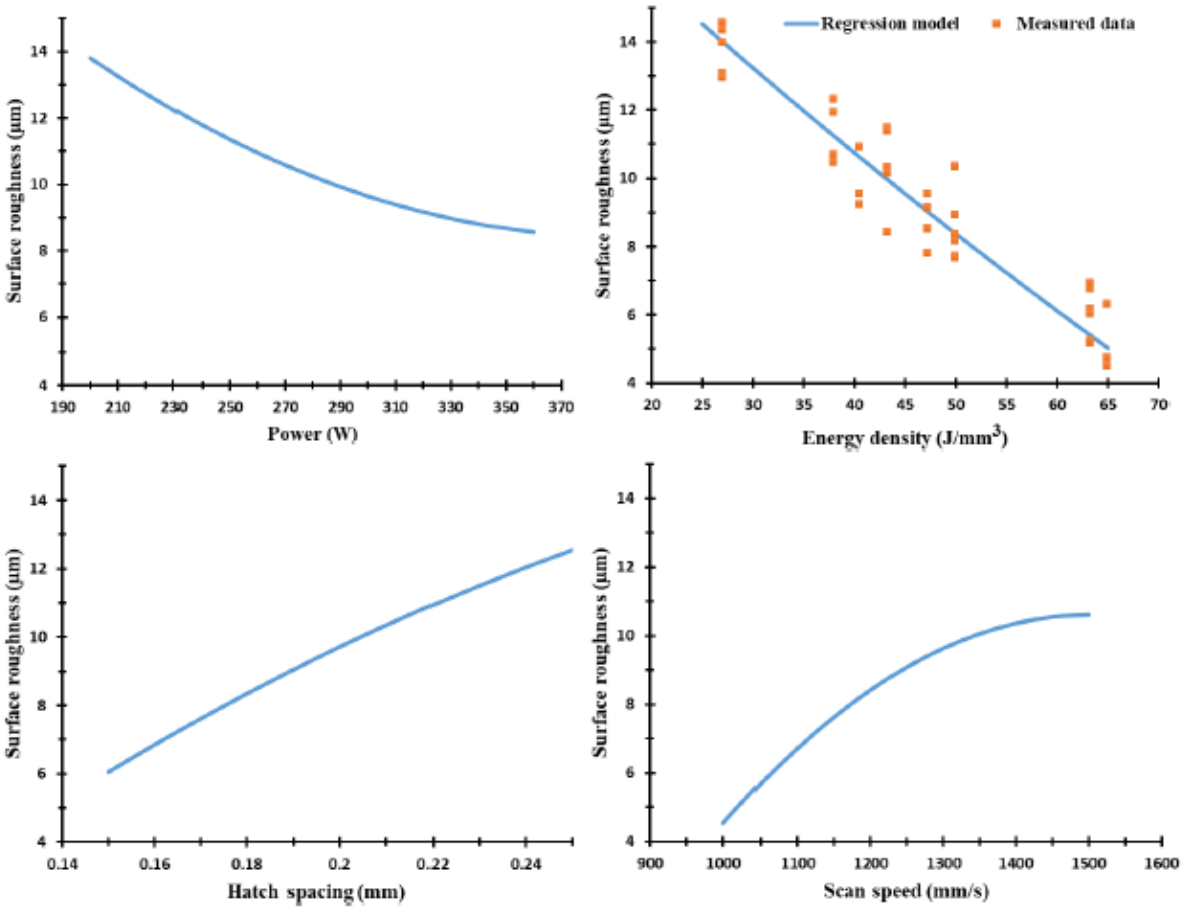

Figure 10: Effect of the SLM process parameters on surface roughness of the as-built AlSi10Mg samples.

322

323 Figure 11 shows that the surface defects of as-built Al6061 parts are more significant than
324 those of the AlSi10Mg parts. These defects are present in the partially melted powder adhering to
325 the surface at a low energy density, surface porosity, and course solidified tracks of laser scanning
326 as illustrated in Figure 11 (a). The surface finish gradually improves as energy density increases
327 from 50 to 123.3 J/mm^3 as illustrated in Figure 11(a-c). In Figure 11(d-f), micro-cracks are also

328 observed at a high microscopic magnification within a size of 50-200 µm, concentrated at the end
329 of the laser tracks along the XY plane due to high thermal stress. These cracks adversely affect the
330 surface roughness of the as-built Al6061 parts, which is why SLM process parameters need to be
331 optimized to reduce micro-crack formation.

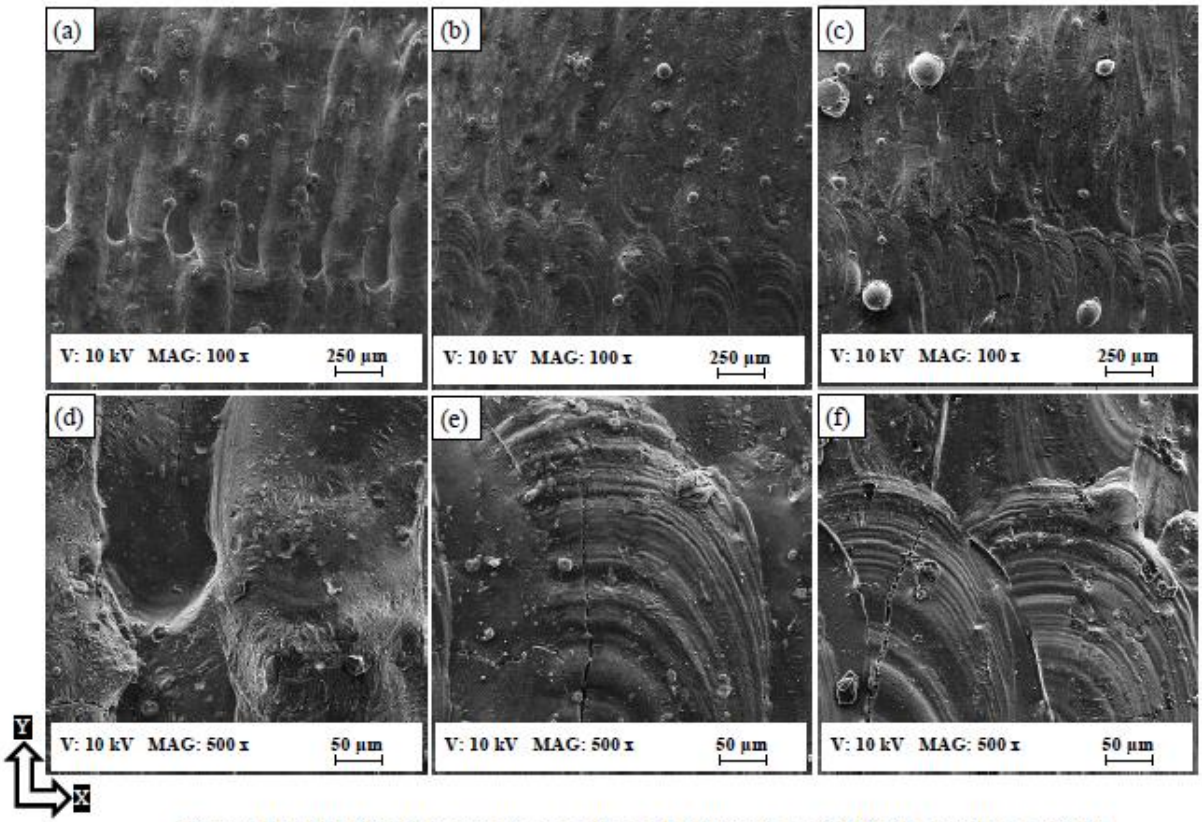

Figure 11: The SEM observations on the as-built surface of Al6061 samples; a, d) 7A, b, e) 14A, c, f) 1A.

332

333 3D surface texture of Al6061 samples in Figure 12 confirms the trend of surface finish
334 improvement from the application of a higher energy density. The energy density range of Al6061
335 (40.5-123.3 J/mm^3) is shifted to a higher value compared to the limited E_d range of the AlSi10Mg
336 alloy (27-65 J/mm^3). This is due to the higher reflectivity and CTE of Al6061 compared to

337 AlSi10Mg, which requires more energy to completely melt the powder layer. However, balling
338 phen

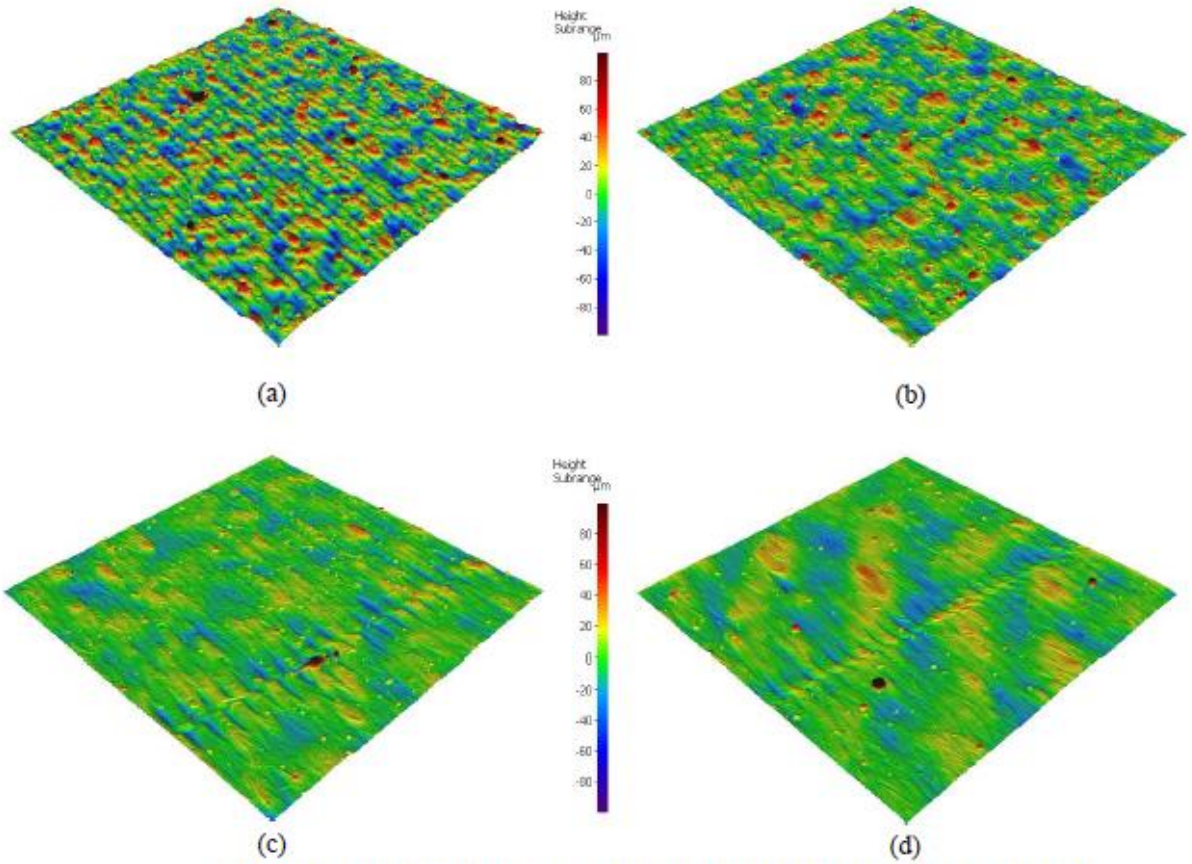

Figure 12: The 3D surface texture of the as-built Al6061 samples; a) 8A, b) 6A, c) 14A, d) 11A.

339

340 omena effect propagates at higher energy densities, limiting the applicable values of E_d.

341 The regression model derived from surface roughness values versus SLM process
342 parameters is presented in Figure 13. The plots illustrate that the higher the laser power, the lower
343 the roughness of the sample surface becomes. The lowest surface roughness of 3 µm was obtained
344 at 370 W laser power, 800 mm/s of scan speed, and 0.15 mm hatch spacing, which is in good
345 agreement with the surface roughness measured for parts fabricated at an energy density of 102.8
346 J/mm^3. In addition, no connection was detected between the effect of laser power on surface

Preprints (www.preprints.org) | NOT PEER-REVIEWED | Posted: 2 November 2018 doi:10.20944/preprints201811.0025.v1

Peer-reviewed version available at Materials 2018, 11, 2343; doi:10.3390/ma11122343

roughness and the change in both scan speed and hatch spacing parameters. However, a substantial relationship was noted between the scan speed and hatch spacing effect on the surface roughness at a constant laser power value. The parabolic shape of the energy density impact indicates an optimum value of 102.8 J/mm^3 which results in a better surface finish.

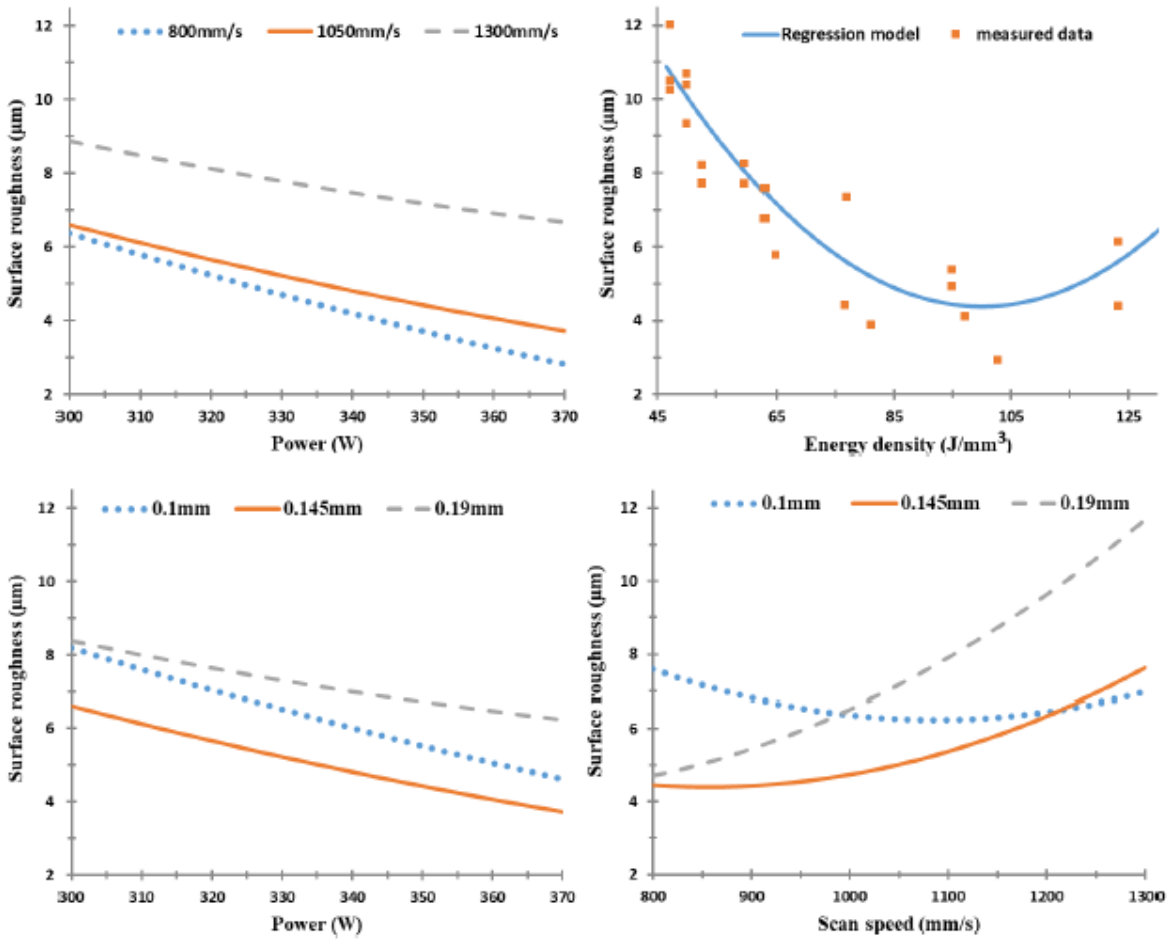

Figure 13: Effect of the SLM process parameters on surface roughness of the as-built Al6061 samples.

3.4 Dimensional accuracy

The dimensional accuracy analysis is performed according to the CMM measurements for both dimensional length tolerance and the top surface flatness of the as-built AlSi10Mg and

Al6061 parts. The values measured along the XY plane were used to generate the regression models which represent the effect of SLM process parameters on each characteristic. Figure 14 shows the dimension tolerance of the average cube length for each sample. According to the recorded results, oversize dimension measurements are compared to the designed values, and there is no contraction observed in the cube sample length. The oversize in the cube length results from the balling effect, partial melted particles on the sample surface, which thus affects the outer surface stair step profile [16]. After excluding the 0.02 mm laser beam offset, the dimension tolerance ranges from 0.15 up to 0.195 mm. Figure 14 shows that hatch spacing is the leading parameter affecting the dimension tolerance accuracy in addition to laser power. The surface flatness difference between the samples tested shows a smaller range of change of 0.035 to 0.09 mm, due to the application of a small 30 µm layer thickness. Figure 15 shows the surface flatness behaviour according to the change of SLM process parameters. It is observed that the hatch spacing and scan speed are the main parameters affecting part surface flatness. The higher the scan speed and hatch spacing, the lower the surface flatness error obtained. Figure 15 also shows a good agreement between the regression model of the energy density effect on surface flatness and the measured values. The results indicate that the surface flatness error increased together with an increase of energy density.

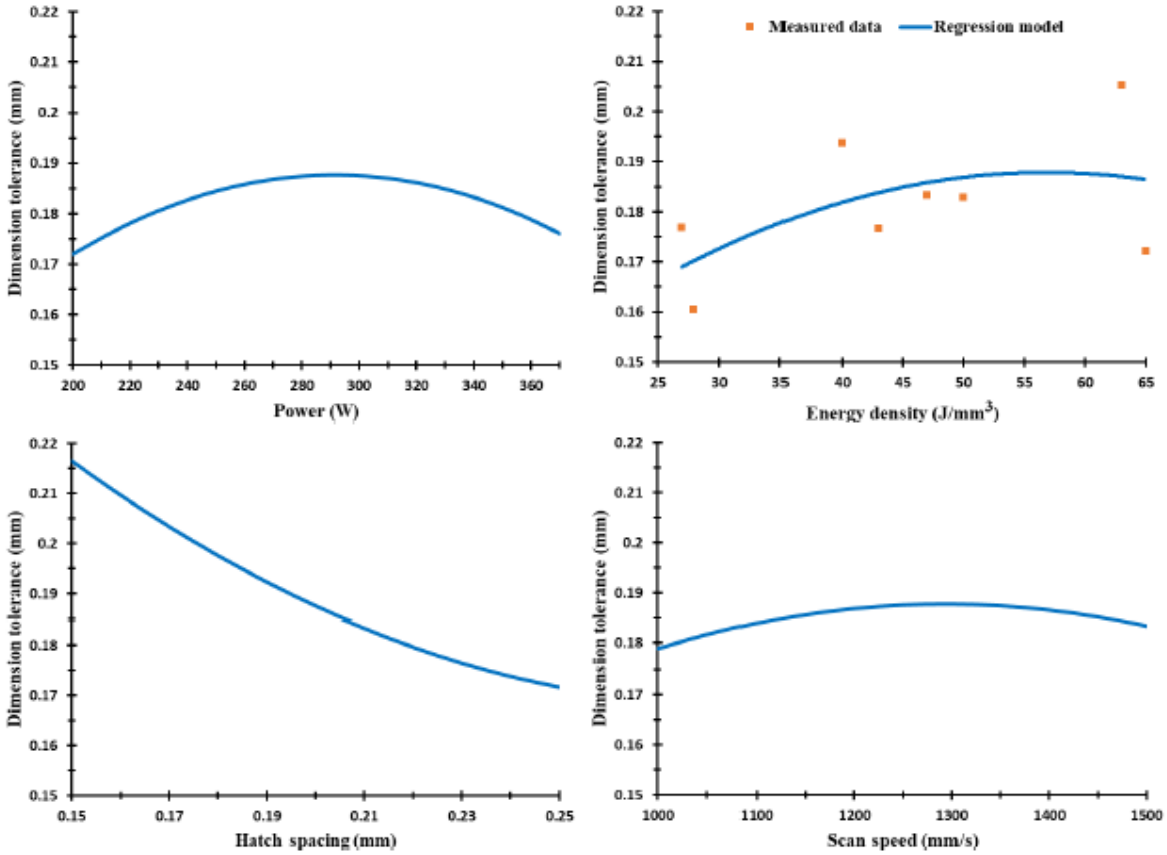

Figure 14: Effect of the SLM process parameters on dimension tolerance of the as-built AlSi10Mg samples.

372

Preprints (www.preprints.org) | NOT PEER-REVIEWED | Posted: 2 November 2018 doi:10.20944/preprints201811.0025.v1

Peer-reviewed version available at Materials 2018, 11, 2343; doi:10.3390/ma11122343

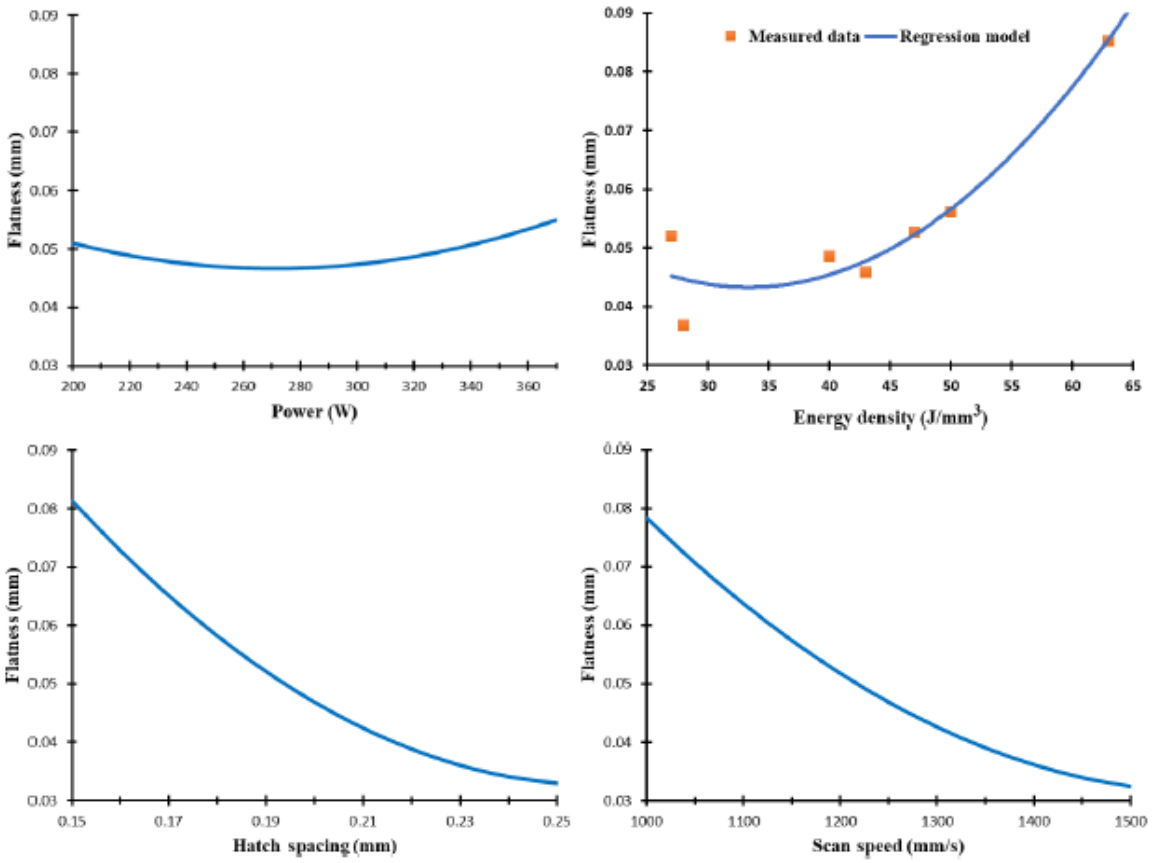

Figure 15: Effect of the SLM process parameters on surface flatness of the as-built AlSi10Mg samples.

373

374 The as-built Al6061 parts show a different behaviour for the dimensional tolerance values
375 than that of AlSi10Mg parts. As illustrated in Figure 16, SLM parameters can affect the dimension
376 tolerance by either expanding or contracting dimensions, and could thus depend on the applied
377 energy density. This might be caused by a change in melt pool dimensions generated by the energy
378 density [16]. The sample dimension tolerance shows a good agreement with the regression model
379 curve. Figure 16 also shows that an energy density higher than 76.8 J/mm^3 results in higher
380 dimension tolerance than the original value. However, energy density applied below this level
381 could lead to part dimension contraction due to the high CTE of Al6061, which results in an

382 increased rate of heat dissipation and solidification. It is also noticed that part contraction occurs
383 at lower rates of hatch spacing and higher scan speeds.

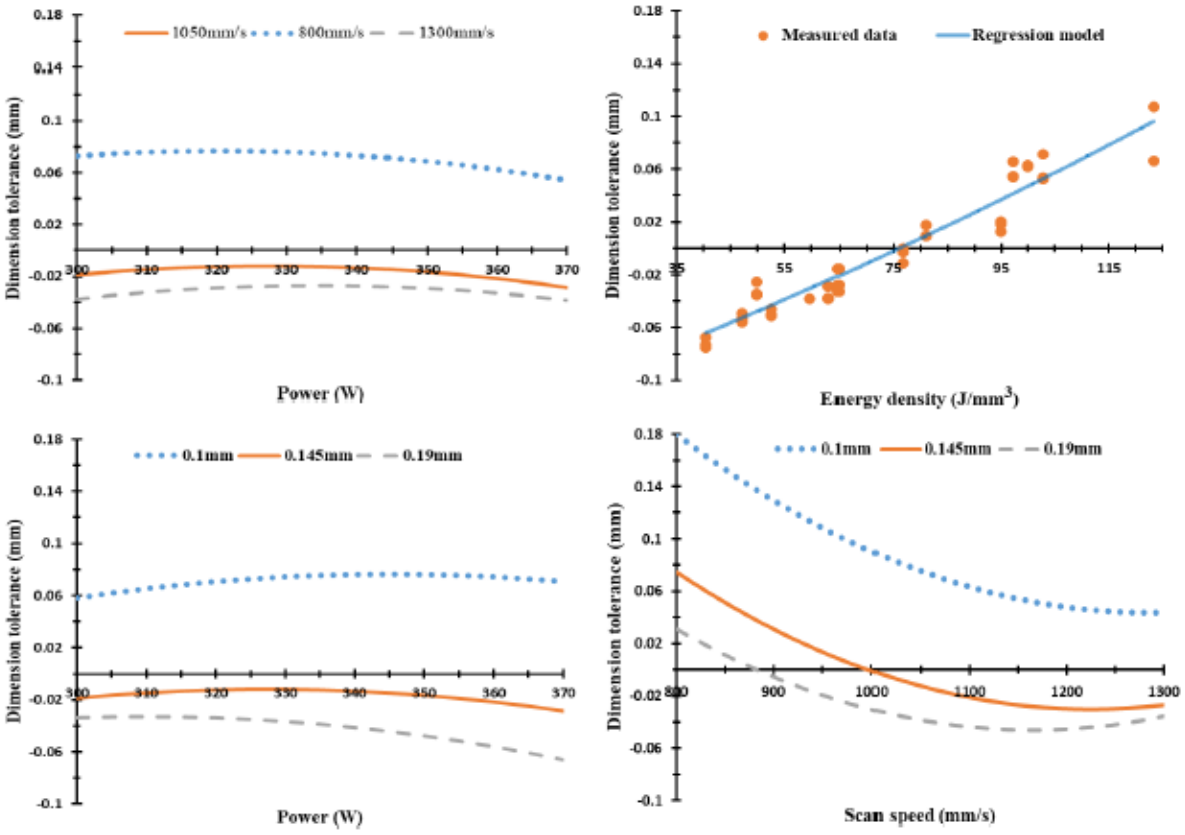

Figure 16: Effect of the SLM process parameters on dimension tolerance of the as-built Al6061 samples.

384

385 In Figure 17, the surface flatness of Al6061 samples demonstrate a range of 0.05 to 0.24
386 mm, which is significantly higher than in the AlSi10Mg sample. This elevated surface flatness
387 disparity might be due to the higher CTE of the Al6061 material which reduces heat accumulation
388 inside the part. This difference in the surface flatness might also result from hot cracks forming
389 inside the part after solidification, low Si content in Al6061, and its high reflectivity of Al6061.

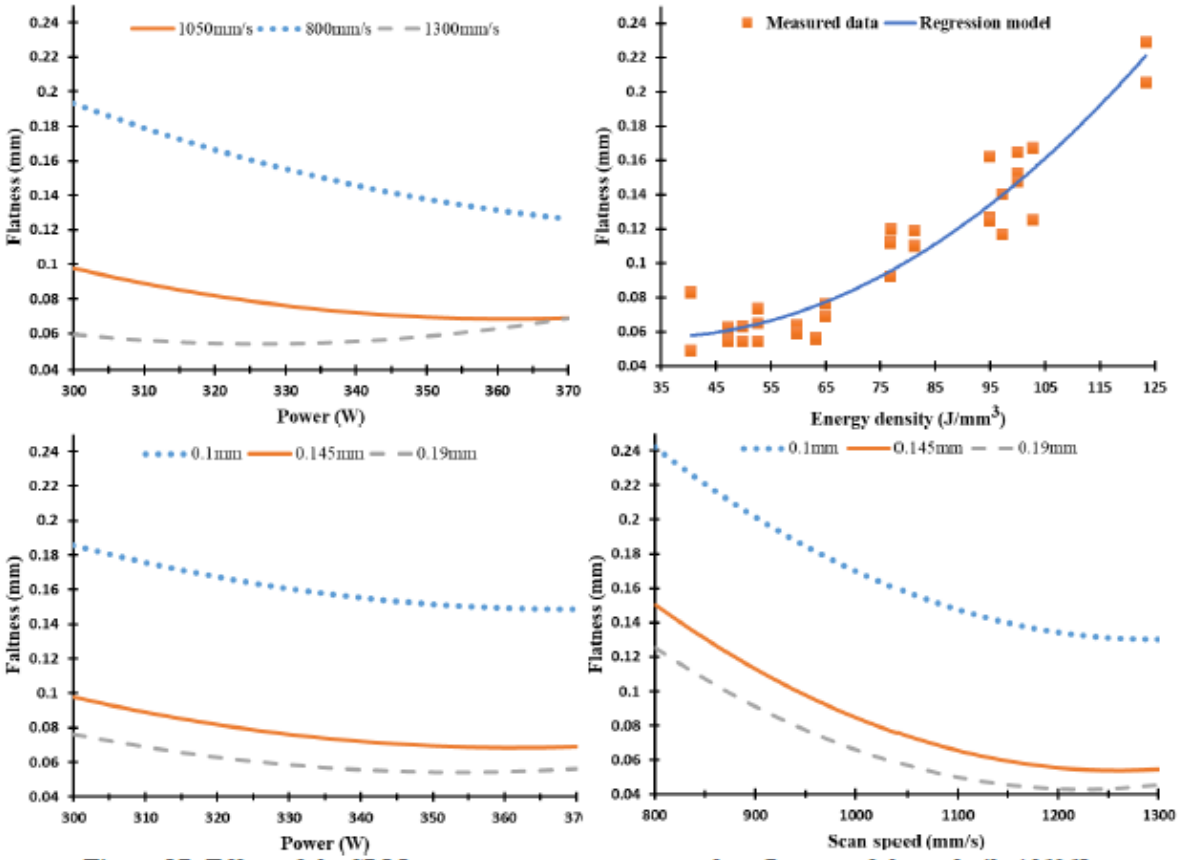

Figure 17: Effect of the SLM process parameters on surface flatness of the as-built Al6061 samples.

A combination of the optimized range for each performance characteristic is presented in the process parameter map of the scan speed and laser power at a constant hatch spacing of 0.19 mm, as illustrated in Figure 18 and Figure 19. The process map for the as-built AlSi10Mg parts is displayed in Figure 18. This map presents an optimized range for the SLM process parameters to satisfy a surface roughness range from 5.5 to 9 µm, relative density within 99.3 to 99.8%, and a range of dimensional tolerance of +0.18 to +0.2 mm.

Preprints (www.preprints.org) | NOT PEER-REVIEWED | Posted: 2 November 2018 doi:10.20944/preprints201811.0025.v1

Peer-reviewed version available at Materials 2018, 11, 2343; doi:10.3390/ma11122343

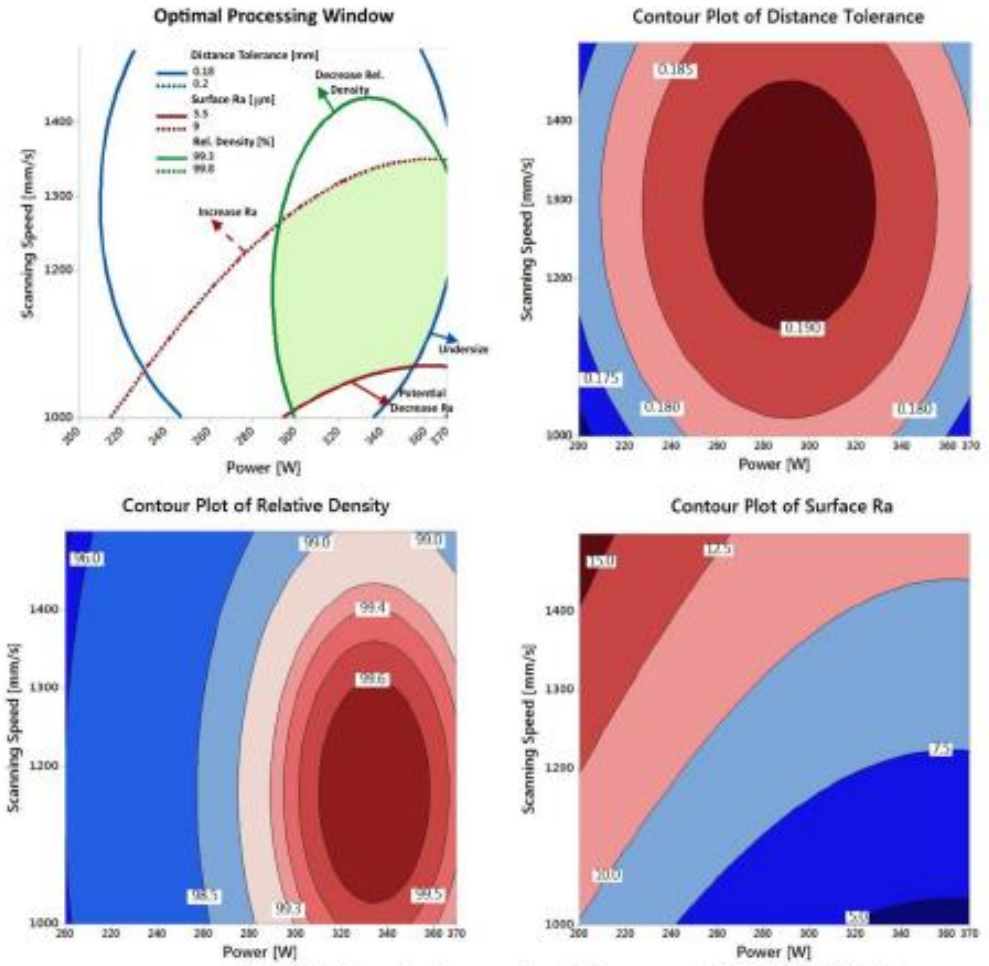

Figure 18: The optimal processing window generated for AlSi10Mg at the hatch spacing value of 0.19 mm.

Figure 19 illustrates the process map for the as-built Al6061 parts that displays the optimized range for the scan speed and the laser power. The optimized process window shows a surface roughness improvement of 3.2 to 6 µm compared to the values obtained from the AlSi10Mg part process map. The dimensional tolerance is also optimized within a smaller range of -0.03 to +0.03 mm with minimum reduction of dimensions compared to the severe contraction in Figure 16 avoided within the optimized process parameter range. However, the relative density of the optimized range has lower values that vary between 98.6 to 98.7%.

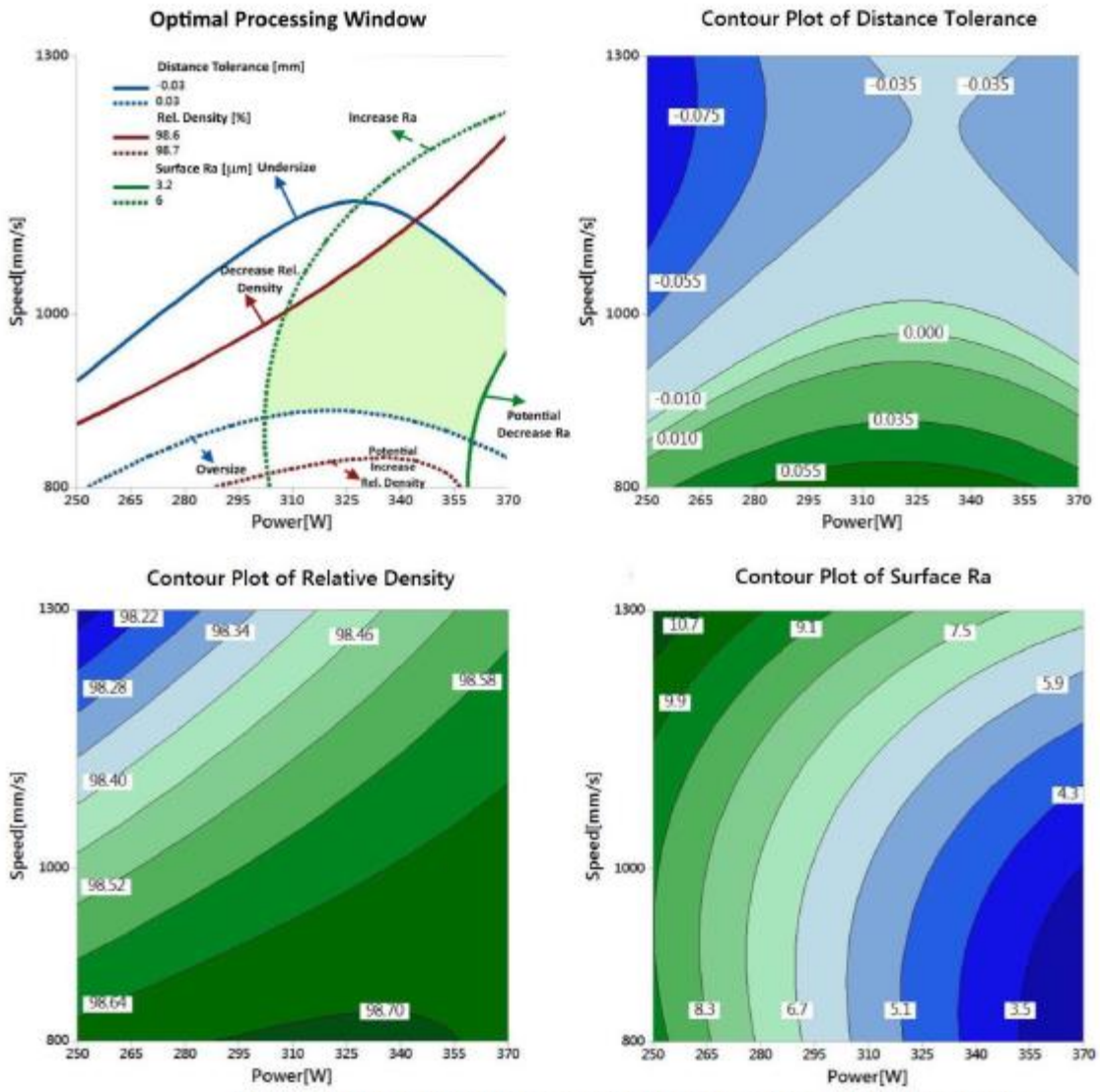

Figure 19: The optimal processing window generated for Al6061 at the hatch spacing value of 0.15 mm.

405

406 **4. Summary and conclusions**

407 The current study represents the first part of a comprehensive work that investigates the
408 effect of SLM process parameters on the quality of the as-built AlSi10Mg and Al6061 parts. A
409 full characterization of both materials' powder was presented. DOE was used to investigate
410 relative density, porosity, surface roughness, surface defects, and dimensional accuracy.

Regression models and the trends were obtained from to the measured data. The results show the following different characteristic behaviours for each material:

1. Powder morphology reveals that AlSi10Mg and Al6061 possess a spherical particle shape interspersed with a considerable percentage of elongated particles. PSD shows a positively skewed distribution within a range of 12 to 120 µm. EDS analysis and XRD phase pattern are used to detect the weight percentage of the chemical elements of each material.
2. The rate of energy density affects the relative density and porosity formation inside the as-built parts. The optimum range of energy density is 50-60 J/mm^3, which results in relative density reaches 99.7%. Relative density of the polished samples reaches 99.9% with a 0.1% internal porosity. The higher rates of energy densities contribute to large hydrogen spherical pores, while the lower rates result in keyhole pores due to the lack of powder fusion.
3. For the Al6061, the maximum relative density measured is 98.72 % using an energy density of 102.8 J/mm^3 and 800 mm/s scan speed. A relationship between the scan speed and laser power was noted, where the higher relative density was achieved at a low scan speed and high laser power. The relative density of the Al6061 parts show lower values compared to those detected in AlSi10Mg, due to lower Si content, which increases the CTE, and causes the formation of hot cracks inside the as-built Al6061 parts.
4. The surface topology is significantly affected by the energy density applied to both materials. The surface roughness reduces alongside the increase of energy density. For the AlSi10Mg samples, the minimum surface roughness is 4.5 µm at 65 J/mm^3. For the Al6061 parts, an energy density of 102.8 J/mm^3 resulted in the best surface roughness of 3 µm. The

energy density is limited to a maximum of 65 J/mm^3 for the AlSi10Mg and 123.3 J/mm^3 for Al6061 to avoid delamination and failure of the part building.

5. For AlSi10Mg, the dimensional tolerance varies between an oversize of 0.15 to 0.195 mm. The best surface flatness could be obtained with higher hatch spacing and scan speeds.

6. For the Al6061 parts, the lowest dimensional tolerance was achieved using an energy density of 76.8 J/mm^3. Contraction of the part dimension was observed at lower energy densities, and the oversized part dimension was detected at higher energy densities. The surface flatness of Al6061 is superior to that of AlSi10Mg parts.

7. Relative density, surface topology, and dimensional accuracy of the as-built AlSi10Mg and Al6061 parts were investigated along with a wide range of SLM process parameters. Optimal processing conditions were determined each material with the goal of achieving a high-quality end product.

8. The influence of the SLM process parameters on microstructure and mechanical properties of as-built AlSi10Mg and Al6061 parts is thoroughly presented in Part II of this study.

Author Contributions:

Formal analysis, Ahmed Maamoun and Yi Xue; Investigation, Ahmed Maamoun and Yi Xue; Methodology, Ahmed Maamoun; Supervision, Mohamed Elbestawi and Stephen Veldhuis; Validation, Ahmed Maamoun; Writing – original draft, Ahmed Maamoun and Yi Xue; Writing – review & editing, Ahmed Maamoun, Mohamed Elbestawi and Stephen Veldhuis.

Acknowledgment

The authors would like to acknowledge the Additive Manufacturing Innovation Centre at Mohawk College, Hamilton, Ontario, Canada and the XRD measurement analysis at McMaster Analytical X-ray (MAX) diffraction facility.

References

1. Manfredi, D.; Calignano, F.; Krishnan, M.; Canali, R.; Paola, E.; Biamino, S.; Ugues, D.; Pavese, M.; Fino, P. Additive Manufacturing of Al Alloys and Aluminium Matrix Composites (AMCs). In *Light Metal Alloys Applications*; 2014 ISBN 978-953-51-1588-5.

2. Srivatsan, T. S.; Sudarshan, T. S. *Additive Manufacturing: Innovations, Advances, and Applications*; 2015; ISBN 9781498714778.

3. Hassanin, H.; Elshaer, A.; Benhadj-Djilali, R.; Modica, F.; Fassi, I. Surface Finish Improvement of Additive Manufactured Metal Parts. *Micro Precis. Manuf.* **2018**, 145–164, doi:10.1007/978-3-319-68801-5_7.

4. Galy, C.; Le Guen, E.; Lacoste, E.; Arvieu, C. Main defects observed in aluminum alloy parts produced by SLM: From causes to consequences. *Addit. Manuf.* 2018, *22*, 165–175.

5. Sufiiarov, V. S.; Popovich, A. A.; Borisov, E. V; Polozov, I. A.; Masaylo, D. V; Orlov, A. V The effect of layer thickness at selective laser melting. *Procedia Eng.* **2017**, *174*, 126–134.

6. Nguyen, Q. B.; Luu, D. N.; Nai, S. M. L.; Zhu, Z.; Chen, Z.; Wei, J. The role of powder layer thickness on the quality of SLM printed parts. *Arch. Civ. Mech. Eng.* **2018**, *18*, 948–955.

7. Cheng, B.; Shrestha, S.; Chou, Y. K. Stress and deformation evaluations of scanning strategy effect in selective laser melting. In *ASME 2016 11th International Manufacturing Science and Engineering Conference*; American Society of Mechanical Engineers, 2016; p. V003T08A009-V003T08A009.

8. Sutton, A. T.; Kriewall, C. S.; Leu, M. C.; Newkirk, J. W. Powder characterisation techniques and effects of powder characteristics on part properties in powder-bed fusion processes. *Virtual Phys. Prototyp.* 2017, *12*, 3–29.

9. Tan, J. H.; Wong, W. L. E.; Dalgarno, K. W. An overview of powder granulometry on feedstock and part performance in the selective laser melting process. *Addit. Manuf.* 2017, *18*, 228–255.

10. Scipioni Bertoli, U.; Guss, G.; Wu, S.; Matthews, M. J.; Schoenung, J. M. In-situ characterization of laser-powder interaction and cooling rates through high-speed imaging

of powder bed fusion additive manufacturing. *Mater. Des.* **2017**, *135*, 385–396, doi:10.1016/j.matdes.2017.09.044.

11. Yang, K. V.; Rometsch, P.; Jarvis, T.; Rao, J.; Cao, S.; Davies, C.; Wu, X. Porosity formation mechanisms and fatigue response in Al-Si-Mg alloys made by selective laser melting. *Mater. Sci. Eng. A* **2018**, *712*, 166–174, doi:10.1016/j.msea.2017.11.078.

12. Read, N.; Wang, W.; Essa, K.; Attallah, M. M. Selective laser melting of AlSi10Mg alloy: Process optimisation and mechanical properties development. *Mater. Des.* **2015**, *65*, 417–424, doi:10.1016/j.matdes.2014.09.044.

13. Aboulkhair, N. T.; Everitt, N. M.; Ashcroft, I.; Tuck, C. Reducing porosity in AlSi10Mg parts processed by selective laser melting. *Addit. Manuf.* **2014**, *1*, 77–86, doi:10.1016/j.addma.2014.08.001.

14. Calignano, F.; Manfredi, D.; Ambrosio, E. P.; Iuliano, L.; Fino, P. Influence of process parameters on surface roughness of aluminum parts produced by DMLS. *Int. J. Adv. Manuf. Technol.* **2013**, *67*, 2743–2751, doi:10.1007/s00170-012-4688-9.

15. Hitzler, L.; Hirsch, J.; Merkel, M.; Hall, W.; Öchsner, A. Position dependent surface quality in selective laser melting: Positionsabhängige Oberflächenqualität im selektiven Laserstrahlschmelzen. *Materwiss. Werksttech.* **2017**, *48*, 327–334, doi:10.1002/mawe.201600742.

16. Han, X.; Zhu, H.; Nie, X.; Wang, G.; Zeng, X. Investigation on selective laser melting AlSi10Mg cellular lattice strut: Molten pool morphology, surface roughness and dimensional accuracy. *Materials (Basel).* **2018**, *11*, doi:10.3390/ma11030392.

17. Maamoun, A. H.; Elbestawi, M.; Dosbaeva, G. K.; Veldhuis, S. C. Thermal Post-processing of AlSi10Mg parts produced by Selective Laser Melting using recycled powder. *Addit. Manuf.* **2018**, *21*, 234–247, doi:10.1016/j.addma.2018.03.014.

18. Maamoun, A.; Elbestawi, M.; Veldhuis, S. Influence of Shot Peening on AlSi10Mg Parts Fabricated by Additive Manufacturing. *J. Manuf. Mater. Process.* **2018**, *2*, 40, doi:10.3390/jmmp2030040.

19. Maamoun, A. H.; Veldhuis, S. C.; Elbestawi, M. Friction stir processing of AlSi10Mg parts produced by selective laser melting. *J. Mater. Process. Technol.* **2019**, *263*, 308–320.

20. Fulcher, B. A.; Leigh, D. K.; Watt, T. J. Comparison of AlSi10Mg and Al 6061 Processed Through DMLS. *Proc. 25th Solid Free. Fabr. Symp.* **2014**, 404–419.

21. Martin, J. H.; Yahata, B. D.; Hundley, J. M.; Mayer, J. A.; Schaedler, T. A.; Pollock, T. M. 3D printing of high-strength aluminium alloys. *Nature* **2017**, *549*, 365–369, doi:10.1038/nature23894.

22. Louvis, E.; Fox, P.; Sutcliffe, C. J. Selective laser melting of aluminium components. *J.*

Mater. Process. Technol. **2011**, *211*, 275–284, doi:10.1016/j.jmatprotec.2010.09.019.

23. Lee, Y. S.; Nandwana, P.; Zhang, W. Dynamic simulation of powder packing structure for powder bed additive manufacturing. *Int. J. Adv. Manuf. Technol.* **2018**, *96*, 1507–1520, doi:10.1007/s00170-018-1697-3.

24. Ma, P.; Prashanth, K.; Scudino, S.; Jia, Y.; Wang, H.; Zou, C.; Wei, Z.; Eckert, J. Influence of Annealing on Mechanical Properties of Al-20Si Processed by Selective Laser Melting. *Metals (Basel).* **2014**, *4*, 28–36, doi:10.3390/met4010028.

25. Olakanmi, E. O. t; Cochrane, R. F.; Dalgarno, K. W. A review on selective laser sintering/melting (SLS/SLM) of aluminium alloy powders: Processing, microstructure, and properties. *Prog. Mater. Sci.* **2015**, *74*, 401–477.

26. Sames, W. J.; List, F. A.; Pannala, S.; Dehoff, R. R.; Babu, S. S. The metallurgy and processing science of metal additive manufacturing. *Int. Mater. Rev.* 2016, *61*, 315–360.

27. Damon, J.; Dietrich, S.; Vollert, F.; Gibmeier, J.; Schulze, V. Process dependent porosity and the influence of shot peening on porosity morphology regarding selective laser melted AlSi10Mg parts. *Addit. Manuf.* **2018**, *20*, 77–89, doi:10.1016/j.addma.2018.01.001.

28. A.A, R.; M.S, W.; M., I.; K., K.; Ahmed, A.; S, S. Mechanical and Physical Properties of AlSi10Mg Processed through Selective Laser Melting. *Int. J. Eng. Technol.* **2016**, *8*, 2612–2618, doi:10.21817/ijet/2016/v8i6/160806217.

29. Thijs, L.; Kempen, K.; Kruth, J. P.; Van Humbeeck, J. Fine-structured aluminium products with controllable texture by selective laser melting of pre-alloyed AlSi10Mg powder. *Acta Mater.* **2013**, *61*, 1809–1819, doi:10.1016/j.actamat.2012.11.052.

30. Siddique, S.; Imran, M.; Wycisk, E.; Emmelmann, C.; Walther, F. Influence of process-induced microstructure and imperfections on mechanical properties of AlSi12 processed by selective laser melting. *J. Mater. Process. Technol.* **2015**, *221*, 205–213, doi:10.1016/j.jmatprotec.2015.02.023.

31. DebRoy, T.; Wei, H. L.; Zuback, J. S.; Mukherjee, T.; Elmer, J. W.; Milewski, J. O.; Beese, A. M.; Wilson-Heid, A.; De, A.; Zhang, W. Additive manufacturing of metallic components – Process, structure and properties. *Prog. Mater. Sci.* 2018, *92*, 112–224.

32. Kou, S. A Simple Index for Predicting the Susceptibility to Solidification Cracking. *Weld. J.* **2015**, *94*, 374s–388s.

33. Foster, S. J.; Carver, K.; Dinwiddie, R. B.; List, F.; Unocic, K. A.; Chaudhary, A.; Babu, S. S. Process-Defect-Structure-Property Correlations During Laser Powder Bed Fusion of Alloy 718: Role of In Situ and Ex Situ Characterizations. *Metall. Mater. Trans. A Phys. Metall. Mater. Sci.* 2018.